Detection of gaseous plumes in IR hyperspectral images using hierarchical clustering

Eitan Hirsch[1] and Eyal Agassi[2,*]

[1]Life Science Research Israel, P. O. Box 19, Nes Ziona 74100, Israel
[2]Israel Institute for Biological Research, P. O. Box 19, Nes Ziona 74100, Israel

*Corresponding author: eyala@iibr.gov.il

The emergence of IR hyperspectral sensors in recent years enables their use in remote environmental monitoring of gaseous plumes. IR hyperspectral imaging combines the unique advantages of traditional remote sensing methods such as multispectral imagery and nonimaging Fourier transform infrared spectroscopy, while eliminating their drawbacks. The most significant improvement introduced by hyperspectral technology is the capability of standoff detection and discrimination of effluent gaseous plumes without need for a clear reference background or any other temporal information. We introduce a novel approach for detection and discrimination of gaseous plumes in IR hyperspectral imagery using a divisive hierarchical clustering algorithm. The utility of the suggested detection algorithm is demonstrated on IR hyperspectral images of the release of two atmospheric tracers. The application of the proposed detection method on the experimental data has yielded a correct identification of all the releases without any false alarms. These encouraging results show that the presented approach can be used as a basis for a complete identification algorithm for gaseous pollutants in IR hyperspectral imagery without the need for a clear background.   © 2007 Optical Society of America

OCIS codes: 280.1120, 100.5010.

1. Introduction

Standoff detection of gaseous plumes by remote infrared technology is a vital technology in environmental monitoring [1–4]. The technology employs the unique spectral absorption spectra that characterize a wide range of molecules in the vapor phase. It delivers an accurate and fast identification and eliminates the need for point sampling in a harsh environment and the inevitable associated risks.

Detection and discrimination methods can be classified by their mission goals. Monitoring smoke stack emissions is aimed to extract quantitative data (usually concentration length) about the effluent gases. In this standoff scenario, the location of the flow source is known and it is continuous. There are numerous measurements and extracting techniques, either ground based or by airborne sensors [5–8]. Detecting fugitive emissions is another application to identify a leak inside large industrial facilities [9]. The most challenging of all applications is the remote detection of hazardous vapors. In this scenario, the sensor is required to indicate the time and the location of a plume in its field of regard without any previous knowledge of when and where such an event will occur.

Until recently, passive detection of gaseous plumes in the atmosphere was only feasible using either nonimaging Fourier transform infrared spectrometers (FTIRs) [3,10] or multispectral imagers [11,12]. Both technologies suffer from serious drawbacks that degrade their performance. While the nonimaging FTIRs allow high spectral resolution measurements, they lack the spatial information that is crucial to achieve reliable detection results. Moreover, the typical fields of view (FOVs) of nonimaging FTIRs are of the order of 1.5°, which leads to low sensitivity at long ranges due to weak signals. Multispectral imagers, on the other hand, have a high spatial resolution but lack a high spectral resolution, which leads to weak spectral signals and difficulties in differentiation
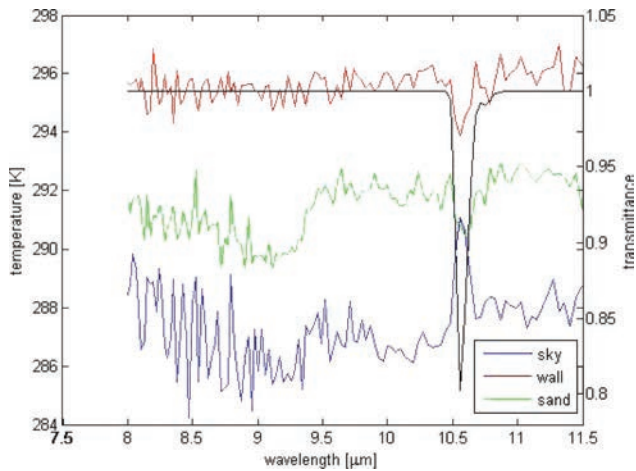
Fig. 1. (Color online) Different background spectra with an SF_6 plume. The SF_6 transmittance spectrum is plotted in black.

among gases. Therefore, algorithms for both sensing technologies that enable the detection and identification of gaseous plumes obtain reliable results only by comparing the scene to a clear reference state. The method of using a clean reference is a major disadvantage, since the sensor FOV must be set before the gas release to allow the system to collect some clear background data.

IR hyperspectral sensors [13–16] combine the unique advantages of traditional remote sensing methods, while eliminating their drawbacks. The most significant improvement introduced by hyperspectral technology is the capability of standoff detection and discrimination of effluent gaseous plumes without requiring a clear reference background or any other temporal information. Detection of gaseous objects differs greatly from detection of hard targets since the plume modifies the spectral signature of the background according to its emission or absorption spectrum. Thus, two pixels in the image that contain the same gaseous plume could have a totally different spectral signature. Furthermore, the gas might affect the spectral signature of the background by either absorption or emission. This complexity of measured spectral signatures is demonstrated in Fig. 1.

The different spectra shown in the figure represent three different background pixels that are overlaid by the gas plume. The gas plume that propagates over the sand and wall backgrounds appears as an absorber, while over the cold sky it appears as an emitter. Additionally, the spectrum of the gas affects only the spectral range in which the gas has significant absorption.

Some approaches to tackle this problem have been suggested in the past, but they all bear significant drawbacks. Matched filtering techniques such as orthogonal and oblique subspace projections [17,18] that are routinely implemented, mainly for small target detection, need background estimation. However, as mentioned before, gas plumes comprise a nonnegligible portion of the FOV of the sensor and they are not opaque, resulting in an inherent mixture of unknown gas plume over the background scene. As a result, estimating the pure background covariance is problematic due to the contamination by the spectral signature of the gas plume. Other detection methods that rely on decomposition of the data cubes are also deficient for the same reason [19]. Some detection methods have been introduced to overcome this ill-posed problem, with a noticeable improvement in the detection performance for weak gas plumes [20–24]. Nevertheless, their performance is severely degraded when intensive plumes are encountered. Clustering was suggested in order to improve the matched filter detection performance [25], with the intention of creating several covariance matrices of different areas in the background, thus creating a matched filter for every cluster. This technique improves the background estimation but inadvertently worsens the effect of the gaseous plume on the background estimation, raising the question of into how many clusters the background should be split. In summary, we look for a detection method that will efficiently detect a semitransparent (either emitter or absorber) object that can comprise a substantial portion of the field of regard of the sensor without any *a priori* knowledge about its location or intensity, and without using any temporal information. Furthermore, we do not know even if the gas plume is actually present in the FOV of the sensor.

In this work we introduce a novel method used to detect and identify gaseous plumes in hyperspectral imagery without any clear background reference, or assumptions about the background. This method is aimed to overcome the difficulties that arise from the inherent mixture of the background and the gas plume spectra. We decompose the scene according to the spectral-spatial information, and we use a physical model to extract the pure transmittance signature of the gas, thus avoiding the need to characterize the background. Section 2 describes our experimental data and setup used to gather the database for algorithm development. The detection algorithm is described in Section 3. We discuss our conclusions in Section 4.

2. Experimental Data

A. Hyperspectral Sensor

The data were collected using the FIRST (Field-Portable Imaging Radiometric Spectrometer Technology) hyperspectral imager manufactured by TELOPS (Québec, Canada) [10]. The sensor couples a Michelson-type interferometer and a mercury cadmium telluride (MCT) focal plane array and produces high spatial-spectral resolution data cubes at a high frame rate. The main features of the FIRST sensor are listed in Table 1.

B. Field Measurements

A small scale field test was conducted to acquire hyperspectral data. The test site was located on a sandy beach. The release point was located at a distance of about 60 m from the imager's observation point. The

Table 1. Technical Parameters of the FIRST Hyperspectral Sensor

Spectral range	8 μm–11.7 μm (850–1250 cm^{-1})
Spectral resolution	0.25–150 cm^{-1}
Focal plane array	256 × 320 pixels
Single pixel FOV	0.35 mrad
Noise equivalent temperature	0.16 °C at 16 cm^{-1}, with binning to 128 × 128
Data rate	~4 s/datacube at 8 cm^{-1}, full spatial resolution

weather conditions, such as air temperature, wind speed, and direction, were measured continuously every second. CHF$_3$ gas (DuPont, 99.995% purity) and SF$_6$ gas (Air Products and Chemicals, 99.99% purity) were released at a steady flow of 1–2 kg/min. The duration of each release was about 1 min, and 12 releases in total were conducted. The weather was windy with partly cloudy skies. Data collection began 1 min prior to every release and lasted 1 min after its end. Figure 2 shows the background scenes. The backgrounds are complex and contain sky, concrete walls, rocks, sand, and vegetation.

3. Detection Method

The formulation of the obtained radiance with the presence of a gaseous plume in the instantaneous field of view (IFOV) of an IR sensor has been extensively studied in the past [1–4,26], and therefore we introduce it very briefly. Atmospheric effects are ignored in our equations, since typical detection ranges are just a few kilometers. At medium spectral resolution the main influence of the atmospheric path is on the signal strength rather on the spectral signature.

The obtained radiance with the presence of a gaseous plume in the instantaneous field of regard of a sensor can be expressed by

$$W(\lambda) = B(\lambda,\ T_{\text{bgd}}) \exp\left[-\alpha(\lambda)\int_0^R C(r)\mathrm{d}r\right] \\ + B(\lambda,\ T_{\text{cld}})\left\{1 - \exp\left[-\alpha(\lambda)\int_0^R C(r)\mathrm{d}r\right]\right\}, \quad (1)$$
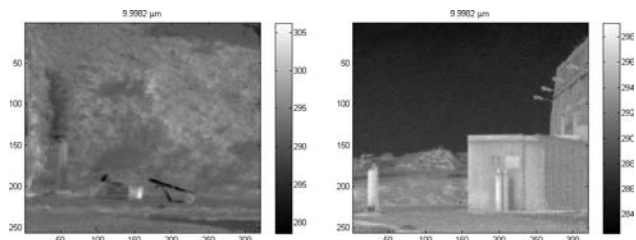
where

Fig. 2. Backgrounds of the different scenes.

$B(\lambda, T_{\text{bgd}})$ is the background radiance at a wavelength of λ and at a distance of R from the sensor. Without a loss in generality we can treat the background as a blackbody radiator with effective temperature T_{bgd}.

$B(\lambda, T_{\text{cld}})$ is Planck's blackbody radiation, corresponding to air temperature T_{cld} at a wavelength of λ.

$\alpha(\lambda)$ is the mass absorption coefficient of a specific tracer gas at a wavelength of λ.

$C(r)$ is the concentration of the tracer gas along the line of sight at a distance of r from the sensor.

We can denote $\tau(\lambda) = \exp[-\alpha(\lambda)\int_0^R C(r)\mathrm{d}r]$ and can express the obtained signal as a blackbody equivalent, $W(\lambda) = B(\lambda, T_s)$, with a temperature of T_s ($T_{\text{air}} \leq T_s \leq T_{\text{bgd}}$). Substituting the appropriate terms and rearranging Eq. (1), we obtain

$$B(\lambda,\ T_s) - B(\lambda,\ T_{\text{cld}}) = \tau(\lambda)[B(\lambda,\ T_{\text{bgd}}) - B(\lambda,\ T_{\text{cld}})].$$
$$(2)$$

Since the temperature differences are small, we can approximate Eq. (2) by linearization of Planck's blackbody radiation with respect to the temperature:

$$(T_s - T_{\text{cld}})\frac{\partial B}{\partial T}\bigg|T_s \approx \tau(\lambda)(T_{\text{bgd}} - T_{\text{cld}})\frac{\partial B}{\partial T}\bigg|T_{\text{bgd}}. \quad (3)$$

Since $\frac{\partial B}{\partial T}\big|T_s \approx \frac{\partial B}{\partial T}\big|T_{\text{bgd}}$ and since all temperature differences are fairly small, we can extract the gas transmission in each wavelength by (other methods to derive similar expression are described in [3,26])

$$\tau(\lambda) = \frac{T_s - T_{\text{cld}}}{T_{\text{bgd}} - T_{\text{cld}}}. \quad (4)$$

Equation (4) shows that, if T_{cld} is known, either by measurement or by estimation, and T_{bgd} is deduced from the scene, we can readily extract τ without use of temporal information; i.e., using the data cubes acquired before the gas was released would yield T_{bgd} for every pixel. However, the purpose of our algorithm is to detect and identify a gaseous plume in a scene, based on a single hyperspectral cube. Hence, instead of using temporal information, T_{bgd} is obtained from the scene under the assumption that, if the gaseous plume covers some background object, the same object will appear in the FOV, which is free of gas as well. The algorithm does not use any prior knowledge of the plume position or any preliminary assumptions on the FOV. The only parameters used by the algorithm are a set of spectral transmittance signatures of several target gases that might be encountered in the scene and the air temperature as measured in the field.

The algorithm has two stages. The first is a divisive hierarchical spectral-spatial decomposition of the hyperspectral image into segments. The second is a spectral analysis of the segments in the scene in order to determine whether some segments contain any gas.
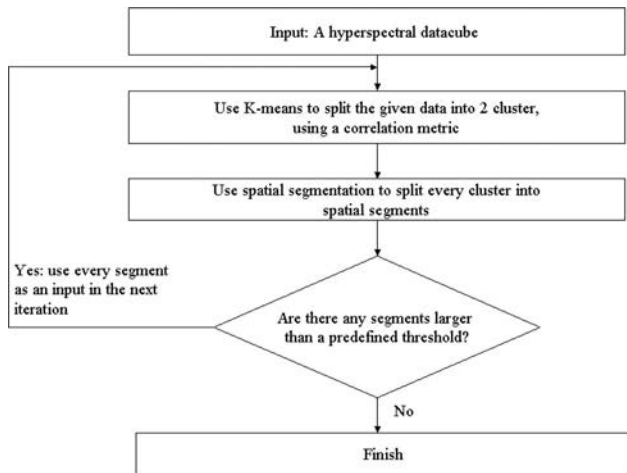
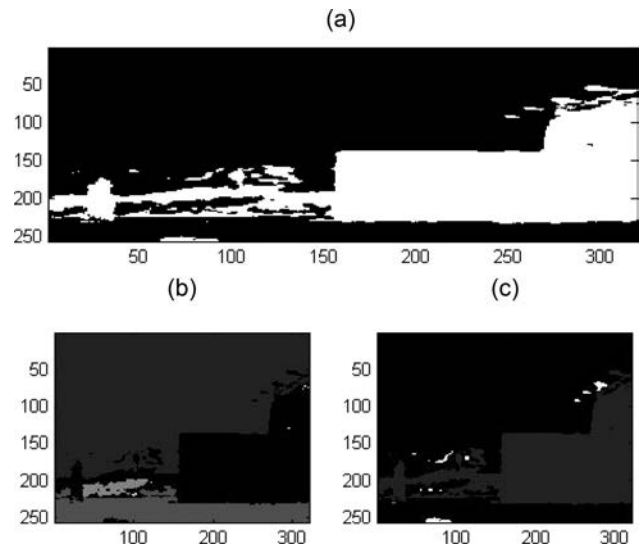Fig. 3. Our divisive hierarchical algorithm scheme.

Fig. 4. Example of the initial spectral-spatial decomposition step: (a) The binary results of the first spectral K-means ($K = 2$). One cluster is colored black and the other is colored white. (b) The result of the spatial segmentation algorithm on the first spectral cluster [black in (a)]. (c) The result of the spatial segmentation algorithm on the second spectral cluster [white in (a)].

A. First Stage—Divisive Hierarchical Spectral-Spatial Decomposition

The decomposition stage assumes that a natural scene tends to be composed of spatial segments containing the same material. Thus we can compress the hyperspectral cube into spectral-spatial segments that represent the scene fairly. As a preprocessing stage, we spatially smooth the hyperspectral image using a two-dimensional (2D) median filter in each spectral band. This procedure eliminates spikes in the hyperspectral cube caused by either bad pixels or imperfect NUC (nonuniformity correction). Then, we decompose the scene by a divisive hierarchical algorithm (Fig. 3): At first, we consider the whole data cube as an input, and at every iteration we use K-means [27] to separate a given area in the scene into two clusters, using a correlation metric; i.e., if $\mathbf{T_1}$ and $\mathbf{T_2}$ are any two spectral signatures acquired by the sensor, the similarity measure between them will be

$$
\begin{aligned}
\text{dist}(\mathbf{T_1}, \mathbf{T_2}) &= 1 - \text{corr}(\mathbf{T_1}, \mathbf{T_2}) \\
&= 1 - \frac{E[(\mathbf{T_1} - \mu_1)(\mathbf{T_2} - \mu_2)]}{\sqrt{E[(\mathbf{T_1} - \mu_1)^2]}\sqrt{E[(\mathbf{T_2} - \mu_2)^2]}},
\end{aligned} \quad (5)
$$

where μ_j is the mean value of $\mathbf{T_j}$. Using this correlation metric ensures that the clusters will be spectrally distinctive, since similar spectra will have lower similarity measure. After each clustering iteration, we spatially segment [28] each cluster: every cluster is divided into spatial segments according to their connectivity. Each of the spatial segments will be given as input to the K-means method for the next iteration. This recursive decomposition continues until all the segments' sizes are smaller than a certain threshold determined by the user. An example of the initial spectral-spatial decomposition step is given in Fig. 4. Figure 4(a) shows the binary result of the first spectral clustering by K-means ($K = 2$); Fig. 4(b) shows the result of the spatial segmentation of the first cluster in (a); Fig. 4(c) shows the result of the

spatial segmentation of the second cluster in Fig. 4(a).

Finally, for each segment the mean spectral signature is calculated. This enables us to consider the scene as a set of segments, each with a unique spectral signature. In Fig. 5, we present an example of this procedure of spatial-spectral decomposition of the scene shown on the right side of Fig. 2. The divisive hierarchical decomposition algorithm is presented in several different stages. One can observe how the scene is separated into smaller segments with every successive iteration.

Another example of the output of the spatial-spectral procedure is shown in Fig. 6. The algorithm has decomposed the scene shown on the left-hand side of Fig. 2 into more than 1600 segments. The spectral separation of the segments is demonstrated in Fig. 7, where the cross-correlation matrix of the spectral signatures of the segments is shown. The (i, j) term in the matrix is given by

$$
\frac{E[(\mathbf{T_i} - \mu_i)(\mathbf{T_j} - \mu_j)]}{\sqrt{E[(\mathbf{T_i} - \mu_i)^2]}\sqrt{E[(\mathbf{T_j} - \mu_j)^2]}}, \quad (6)
$$

where $\mathbf{T_i}$ is the mean spectral signature of the ith segment, and μ_i is the mean of $\mathbf{T_i}$. Our divisive spectral-spatial decomposition algorithm ensures that, even if some of the segments have spectral resemblance to each other (as shown by high values in Fig. 7), they are spatially separated.

The next stage of the detection process is detecting and identification the plume by analyzing the spatial-spectral segments, as presented in Subsection 3.B.
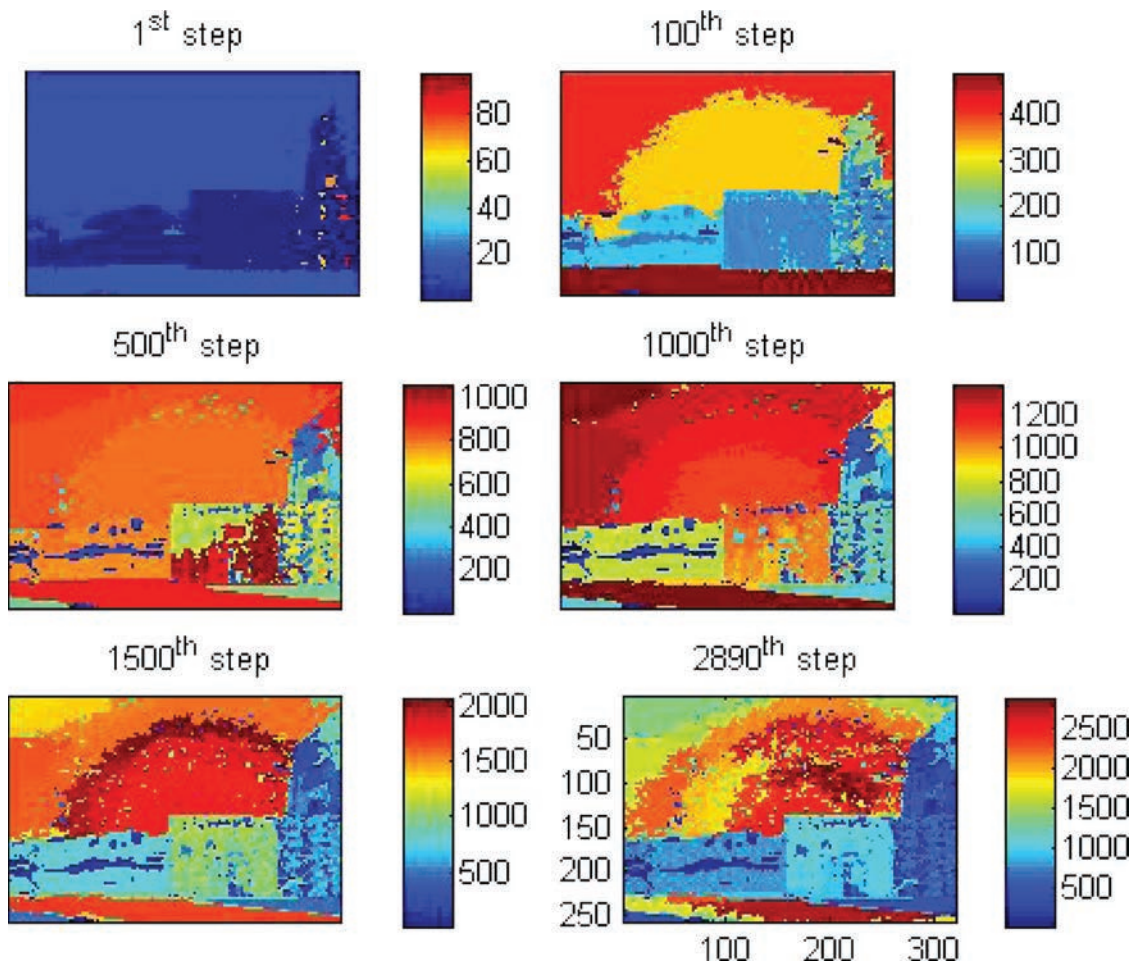
Fig. 5. (Color online) Image segmentation after successive numbers of iterations of the divisive hierarchical spatial-spectral decomposition algorithm.

B. Second Stage—Detection and Identification of the Plume

Since no prior knowledge is used to analyze the scene, every segment might contain a gas plume signature. As stated earlier, instead of using temporal information, we assume that, if the gaseous plume covers some background object, the same object will appear in the FOV, which is free of gas as well (or with substantial different transmissions) as illustrated in Fig. 8.

Therefore, every segment's signature is used twice: once as T_s and once as T_{bgd} [see Eq. (4)]. Figure 9 illustrates the scheme of the second stage of the algorithm. In practice, we use each segment's signature
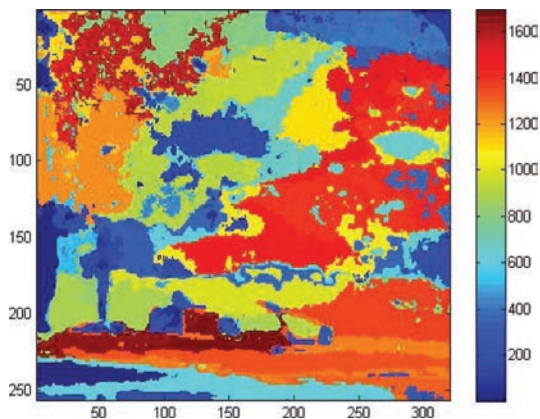

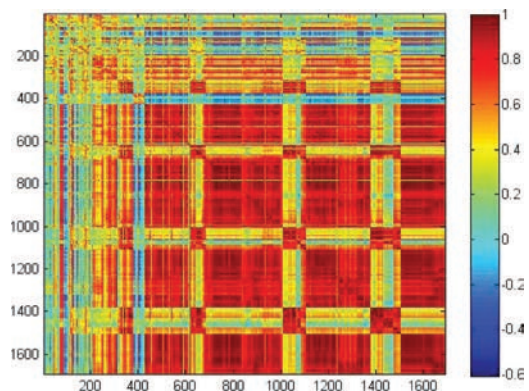Fig. 6. (Color online) Final result of the spatial-spectral decomposition algorithm on one of the scenes.

Fig. 7. (Color online) Spectral cross-correlation matrix of the various segments. High correlation values indicate spectrally similar segments, but our algorithm ensures they are spatially separated.
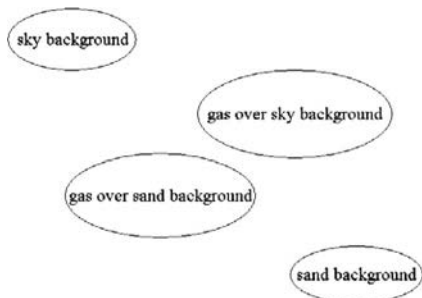
Fig. 8. Illustration of the detection algorithm assumption.

Fig. 10. (Color online) Result of the identification stage of the detection algorithm for CHF_3 and SF_6 plumes, released simultaneously.

as T_s and calculate the spectral transmittance when T_{bgd} are all the other segments signatures. This step produces $n - 1$ possible transmission spectra for each segment, where n is the number of segments obtained in the first step of the algorithm. The correlations (dot product) between each calculated transmittance spectrum and the spectral signatures of the target gases compounds are calculated. For every segment and for every target signature the maximum correlation value is considered. At the end of this procedure, every segment is attached with a correlation value for each gas target. A correlation value higher than a predefined threshold leads to classification of the segment as containing a specific target gas. One should notice that using Eq. 4 allows us to use simple dot product for the classification of the gas, since the produced transmission spectra (τ) eliminate the background spectral features.

Figure 10 shows the result of the identification process for CHF_3 and SF_6, which had been released simultaneously. The algorithm was operated over 114 hyperspectral cubes, in two different backgrounds. As mentioned in Section 2, some of the cubes did not contain any plumes while others contained either plumes of CHF_3, SF_6, or a mixture of both. Applying the proposed detection method over the experimental data yielded a correct identification in all the releases without any false positives (i.e., indication of a plume
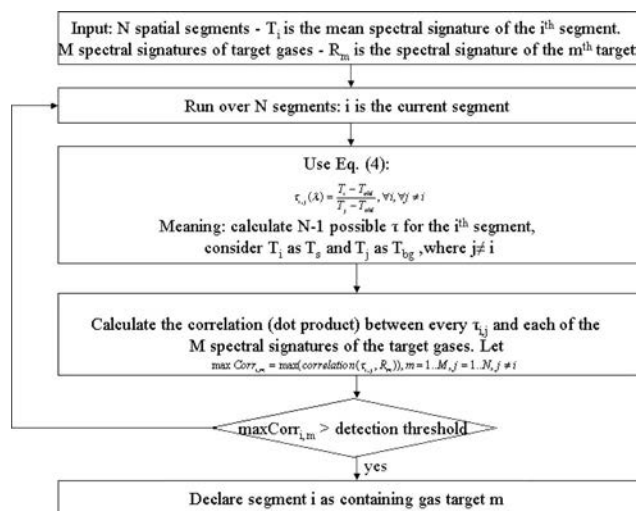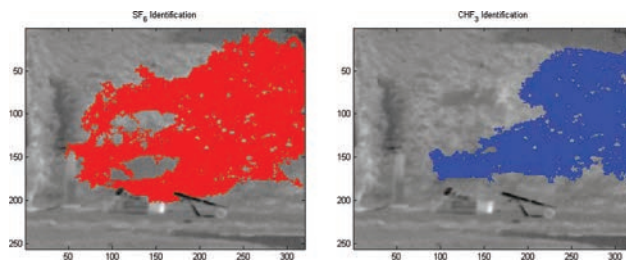
when it is not present in the FOV of the sensor). Furthermore, the algorithm yielded identification of both tracers whenever they were present as a mixture. These encouraging results show that the presented approach can be used as a core for a complete identification algorithm for gaseous pollutants in IR hyperspectral imagery without the need for a clean background. Further work over large databases at various backgrounds and thermal contrasts is still needed to verify and validate the proposed detection and identification method. There is also a need for appropriate quantitative metrics in order to evaluate its performance as a function of the signal strength.

4. Conclusions

A novel algorithm for detection and classification of gaseous plumes in hyperspectral images without relying on clear reference background has been introduced. This detection method does not use any *a priori* assumption about the size or the position of the gas plume. The proposed algorithm exploits the high spectral and spatial resolution of the sensor to decompose the hyperspectral cube into small segments, which are used to detect and classify the plume. The detection algorithm overcomes the inherent mixture of the plume and the background spectra, which is considered the main obstacle for a reliable detection scheme that does not use any ancillary knowledge or assumptions (e.g., temporal data). Applying the proposed detection method over the experimental data has yielded a correct identification in all the releases without any misclassifications. Further work over large databases at various backgrounds and thermal contrasts is still needed to verify and validate the proposed detection and identification method. There is also need for an appropriate quantitative metric in order to evaluate its performance as a function of the signal strength. Optimization of algorithm performance in terms of run time versus detection results is also needed.

Fig. 9. Second stage of the algorithm scheme.

References

1. D. F. Flanigan, "Vapor-detection sensitivity as a function of spectral resolution for a single Lorentzian band," Appl. Opt. **34,** 2636–2639 (1995).
2. D. F. Flanigan, "Prediction of the limits of detection of hazardous vapors by passive infrared with the use of MODTRAN," Appl. Opt. **35,** 6090–6098 (1996).
3. M. L. Polak, J. L. Hall, and K. C. Herr, "Passive Fourier-transform infrared spectroscopy of chemical plumes: an

algorithm for quantitative interpretation and real-time background removal," Appl. Opt. **34,** 5406–5412 (1995).

4. A. Hayden, E. Niple, and B. Boyce, "Determination of trace-gas amounts in plumes by the use of orthogonal digital filtering of thermal-emission spectra," Appl. Opt. **35,** 2802–2809 (1996).

5. S. J. Young, "Detection and quantification of gases in industrial-stack plumes using thermal-infrared hyperspectral imaging," Tech. Rep. ATR-2002(8407)-1 (The Aerospace Corporation, 2002).

6. D. W. Messinger, "Gaseous plume detection in hyperspectral images: a comparison of methods," Proc. SPIE **5425,** 592–603 (2004).

7. J. S. McGonigle, C. L. Thomson, V. I. Tsanev, and C. Oppenheimer, "A simple technique for measuring power station SO_2 and NO_2 emissions," Atmos. Environ. **38,** 21–25 (2001).

8. R. C. Carlson, A. F. Hayden, and W. B. Telfair, "Remote observations of effluents from small building smokestacks using FTIR spectroscopy," Appl. Opt. **27,** 4952–4959 (1988).

9. J. Sandsten, H. Edner, and S. Svanberg, "Gas visualization of industrial hydrocarbon emissions," Opt. Express **12,** 1443–1451 (2004).

10. R. Harig, G. Matz, P. Rusch, H. H. Gerhard, and J. H. Gerhard, "New scanning infrared gas imaging system (SIGIS 2) for emergency response," Proc. SPIE **5995,** 174–181 (2006).

11. E. Agassi and E. Hirsch, "Remote detection of SF_6 plumes in a stable boundary layer," Proc. SPIE **5988,** 131–141 (2006).

12. L. Grenier, G. Pelous, and P. Adam, "Passive stand-off detection of gas clouds in open field by IR imagery," Proc. SPIE **3553,** 86–92 (1998).

13. Y. Guern, L. Grenier, and F. Carpentier, "Uncooled IRFPA for low-cost multispectral/hyperspectral LWIR imaging device," Proc. SPIE **5093,** 126–135 (2003).

14. M. Hinnrichs and B. Piatek, "Hand held hyperspectral imager for chemical/biological and environmental applications," Proc. SPIE **5270,** 10–18 (2003).

15. V. Farley, A. Vallières, M. Chamberland, and J. Legault, "Performance of the FIRST, a longwave infrared hyperspectral imaging sensor," Proc. SPIE **6398** (2006).

16. W. J. Marinelli, C. M. Gittins, A. H. Gelb, and B. D. Green, "A tunable Fabry–Perot etalon-based long-wave infrared imaging spectroradiometer," Appl. Opt. **38,** 2594–2604 (2000).

17. J. C. Harsanyi and C.-I. Chang, "Hyperspectral image classification and dimensionality reduction: an orthogonal subspace projection," IEEE Trans. Geosci. Remote Sens. **32,** 794–795 (1994).

18. R. T. Behrens and L. L. Scharf, "Signal processing applications of oblique projection operators," IEEE Trans. Signal Process. **42,** 1413–1424 (1994).

19. A. Iffarraguerri and C. Gittins, "Chemical cloud mapping and identification using convex cone analysis of AIRIS multispectral imaging data," Proc. SPIE **3533,** 114–121 (1998).

20. T. Burr and B. R. Foy, "Characterizing clutter in the context of detecting weak gaseous plumes in hyperspectral imagery," Sensors **6,** 1587–1615 (2006).

21. T. Burr and N. Hegarther, "Overview of physical models and statistical approaches for weak gaseous plume detection using passive infrared hyperspectral imagery," Sensors **6,** 1721–1750 (2006).

22. J. Theiler, B. R. Foy, and A. M. Fraser, "Nonlinear signal contamination effects for gaseous plume detection in hyperspectral imagery," Proc. SPIE **6233,** 62331U (2006).

23. J. Theiler, B. R. Foy, and A. M. Fraser, "Characterizing non-Gaussian clutter and detecting weak gaseous plumes in hyperspectral imagery," Proc. SPIE **5806,** 182–193 (2005).

24. J. Theiler and B. R. Foy, "The effect of signal contamination in matched-filter detection of the signal on a cluttered background," IEEE Geosci. Remote Sens. Lett. **3,** 98–102 (2006).

25. C. T. Funk, J. Theiler, D. A. Roberts, and C. C. Boerl, "Clustering to improve matched filter detection of weak gas plumes in hyperspectral thermal imagery," IEEE Trans. Geosci. Remote Sens. **39,** 1410–1420 (2001).

26. A. Beil, R. Daum, R. Harig, and G. Matz, "Remote sensing of atmospheric pollution by passive FTIR spectroscopy," Proc. SPIE **3493,** 32–43 (1998).

27. R. Duda, P. Hart, and D. Stork, *Pattern Classification,* 2nd ed. (Wiley, 2001).

28. B. Jahne, *Digital Image Processing* (Springer-Verlag, 1997).